frontiers | Frontiers in Earth Science

ORIGINAL RESEARCH
published: 04 July 2022
doi: 10.3389/feart.2022.934488

Distribution Characteristics and Genesis of Marine Anoxic Conditions in the Southwest of the Upper Yangtze Basin During the Late Ordovician–Early Silurian, South China

*Zaitian Dong[1,2], Zetang Wang[1,2], Wenli Zhang[3,4], Shaoning Cheng[4], Xuehai Fu[1,2] and Chaoyong Wang[1,2]**

[1]Key Laboratory of CBM Resources and Dynamic Accumulation Process, China University of Mining and Technology, Ministry of Education, Xuzhou, China, [2]School of Resources and Earth Science, China University of Mining and Technology, Xuzhou, China, [3]Xi'an University of Science and Technology, Xi'an, China, [4]School of Health, Yuncheng Vocational and Technical University, Yuncheng, China

The distribution characteristics and formation of marine anoxic conditions through the Late Ordovician–Early Silurian (O–S) remain poorly resolved despite their importance in the preservation of sedimentary organic matter and the formation of black shale. In this study, the major, trace, and pyrite $\delta^{34}S$ ($\delta^{34}S_{py}$) contents of 36 shale samples at the edge of the southwest depocenter of the Upper Yangtze Basin (Tianlin and Changhebian sections) were analyzed to understand the redox conditions, terrigenous clastic inputs, and primary productivity changes. The iron speciation and enrichment factor of U and Mo show that the range of anoxic conditions gradually expanded from the sedimentation center to the edge during the late Katian stage, peaked in the early Hirnantian stage followed by a rapid decrease, and expanded again during the early Rhuddanian stage. Comprehensive index analysis showed that the increase of terrigenous clastic input and the relative decrease of primary productivity due to tectonism and sea level change controlled the transformation of the water column from anoxic, especially euxinic, to suboxic-oxic conditions. This is reflected in the correlation between paleo-salinity, $\delta^{34}S_{py}$, chemical index of alteration, and the organic carbon accumulation rate. This work emphasizes the control of terrigenous clastic input and sulfate availability on the transformation of marine redox conditions during the O-S period in semi-restricted basins.

Keywords: redox conditions, paleo-salinity, accumulation rate of organic matter, upper yangtze basin, late ordovician–early silurian

OPEN ACCESS

Edited by:
Dongdong Liu,
China University of Petroleum, Beijing, China

Reviewed by:
Haichao Wang,
Xinjiang University, China
Jienan Pan,
Henan Polytechnic University, China

****Correspondence:***
Chaoyong Wang
wangcy@cumt.edu.cn

Specialty section:
This article was submitted to Economic Geology, a section of the journal Frontiers in Earth Science

Received: *02 May 2022*
Accepted: *27 May 2022*
Published: *04 July 2022*

Citation:
Dong Z, Wang Z, Zhang W, Cheng S, Fu X and Wang C (2022) Distribution Characteristics and Genesis of Marine Anoxic Conditions in the Southwest of the Upper Yangtze Basin During the Late Ordovician–Early Silurian, South China. Front. Earth Sci. 10:934488. doi: 10.3389/feart.2022.934488

1 INTRODUCTION

The transition from Late Ordovician to Early Silurian (O–S) was an important event in Earth's history. This period witnessed several occurrences, such as the Hirnantian glaciation, biological extinction and recovery, structural changes, volcanic activities, and marine environmental changes (Adachi et al., 1986; Brenchley et al., 2003; Yan et al., 2009; Delabroye and Vecoli, 2010; Yan et al., 2010; Algeo et al., 2016). Among them was the widespread deposition of black shales, which are an important source of shale gas (Luening et al., 2000; Zou et al., 2016). Such widespread formation of

black shales can be attributed to primary productivity and a marine anoxic environment (namely paleoproductivity and preservation modes) (Sageman et al., 2003; Gallego-Torres et al., 2007; Mort et al., 2007; Ge et al., 2020). According to the productivity model, the advancement and extinction of glaciers promoted the release of terrestrial nutrients (e.g., phosphorus and iron) into the ocean causing numerous oceanic phytoplankton to flourish (Saltzman and Young, 2005). Higher primary productivity and organic carbon sinks contributed to the formation of black shale. The preservation model suggests that anoxic water effectively slowed the consumption of organic matter (OM), increased its burial flux, and promoted the formation of black shale (Algeo and Maynard, 2004). Studies have shown that the anoxic water column may be the main controlling factor in black shale formation and biological extinction as compared to higher primary productivity (Hammarlund et al., 2012; Gomes and Hurtgen, 2015; Liu et al., 2016; Zou et al., 2018; Li et al., 2019; Li N. et al., 2021; Pan et al., 2021; Wang et al., 2021).

The black shales of the Upper Yangtze Basin, South China, formed between Late Ordovician [Katian, Wufeng Formation, (WF)] and Silurian [Telychian, Longmaxi Formation, (LMX)]. Existing studies on lithofacies paleogeography show that semi-limited and limited water environments appeared in the northeast and southwest Upper Yangtze Basin owing to tectonism and sea-level fluctuations, respectively, forming two relatively independent depocenters, which controlled the transformation of redox conditions in the water column (Liang et al., 2009). Zou et al. (2018) and Li et al. (2019) emphasized the controlling effect of sulfate availability on the development of anoxic water, especially euxinic conditions from different depths and offshore distances. Li Y. et al. (2021) highlighted the contribution of volcanism to primary productivity and the preservation of OM. However, the mechanism of this control is unclear. In addition, the influence of frequent volcanic activity and extensive glaciers on the transformation of redox conditions in the water column of the Upper Yangtze Basin has not been studied comprehensively and needs further discussion.

To explore the controlling factors of marine redox conditions and the formation of OM in the Upper Yangtze Basin during the O–S period, we analyzed the whole-rock major, trace elements, and sulfur isotopes ($\delta^{34}S_{py}$). Combined with previously published data on the Shuanghe section, which is located in the southwest depocenter, we reconstructed the redox evolution of marine water in the southwest of the Upper Yangtze Basin and evaluated the extent of its control on the formation of black shales.

2 GEOLOGICAL SETTING

Located west of the South China Block, the Upper Yangtze Basin is a superimposed basin controlled by peripheral tectonic activity (Zhou et al., 2015). During the O–S period, the South China Block comprised the Cathaysian and Yangtze Blocks. These blocks converged to form an intracontinental orogeny that led to the formation of the surrounding areas (Kangdian-Qianzhong Uplift, Hanzhong Uplift, and Chuanzhong Uplift surround the Upper Yangtze Basin) isolating the Upper Yangtze Basin from the high seas, and form a semi-restricted shallow-sea basin (Chen et al., 2004; Mu et al., 2011) (**Figure 1A**).

The Changhebian (28°44′33″ N and 103°26′23″ E) and Tianlin (27°55′15″ N and 105°36′45″ E) sections, located in the southwest Upper Yangtze Basin and adjacent to the Chuanzhong and Qianzhong Uplifts on both sides of the depocenter, respectively, were selected for this study (**Figure 1B**). The selected sections were compared with the Shuanghe section, which is located in the southwest depocenter. The Shuanghe section has been studied extensively in terms of biostratigraphy, paleogeography, and chemical stratigraphy (Liu et al., 2016; Lu et al., 2021). The stratigraphic sequences of the three sections are similar during the O–S period. The WF, Guanyinqiao (GYQ), and LMX Formations are distributed evenly in the Tianlin and Shuanghe sections (**Figure 1C**) whereas, only the WF and LMX Formations are identified in the Changhebian section (**Figure 1C**). The WF and LMX Formations comprise organic-rich black shales and abundant graptolite fossils. The GYQ Formation mainly comprises carbonaceous limestone, with abundant fossil shells that record the decline of sea level. Graptolite strata and regional-global zoning schemes of O–S have been established in the study area as the biostratigraphic control (Zhou et al., 2015; Li et al., 2019; Wang et al., 2021).

3 SAMPLES AND METHODS

3.1 Samples

In total, 23 and 13 representative fresh shale samples were collected from the Tianlin and Changhebian sections, respectively. All samples were ground to ≤ 200 mesh size using a tungsten carbide crusher.

3.2 Methods

For total organic carbon (TOC) measurements, all samples were leached with ≥ 20% HCl to remove the carbonate content and washed with distilled water before analysis. A LECO CS230 carbon sulfur analyzer at the China University of Mining and Technology Advanced Analysis and Computation Center was used to determine the dried residues and unacidified samples.

Major element analyses were conducted at the China University of Mining and Technology Advanced Analysis and Computation Center using a Bruker S8 Tiger X-ray fluorescence spectrometer (XRF). Trace elements were tested at the Jiangsu Geological and Mineral Resources Design and Research Institute using a PE Elan600 standard inductively coupled plasma mass spectrometer (ICP-MS). Sedimentary Fe speciation and S isotopes of pyrite ($\delta^{34}S_{py}$) were tested at the State Key Laboratory of Biogeology and Environmental Geology, China. The detailed test methods and standards can be found in the study by Wang et al. (2021).

3.3 Proxies Used in This Study

The chemical index of alteration (CIA) and component variability index (ICV) can be used to determine the intensity of chemical weathering and composition of sediments in the

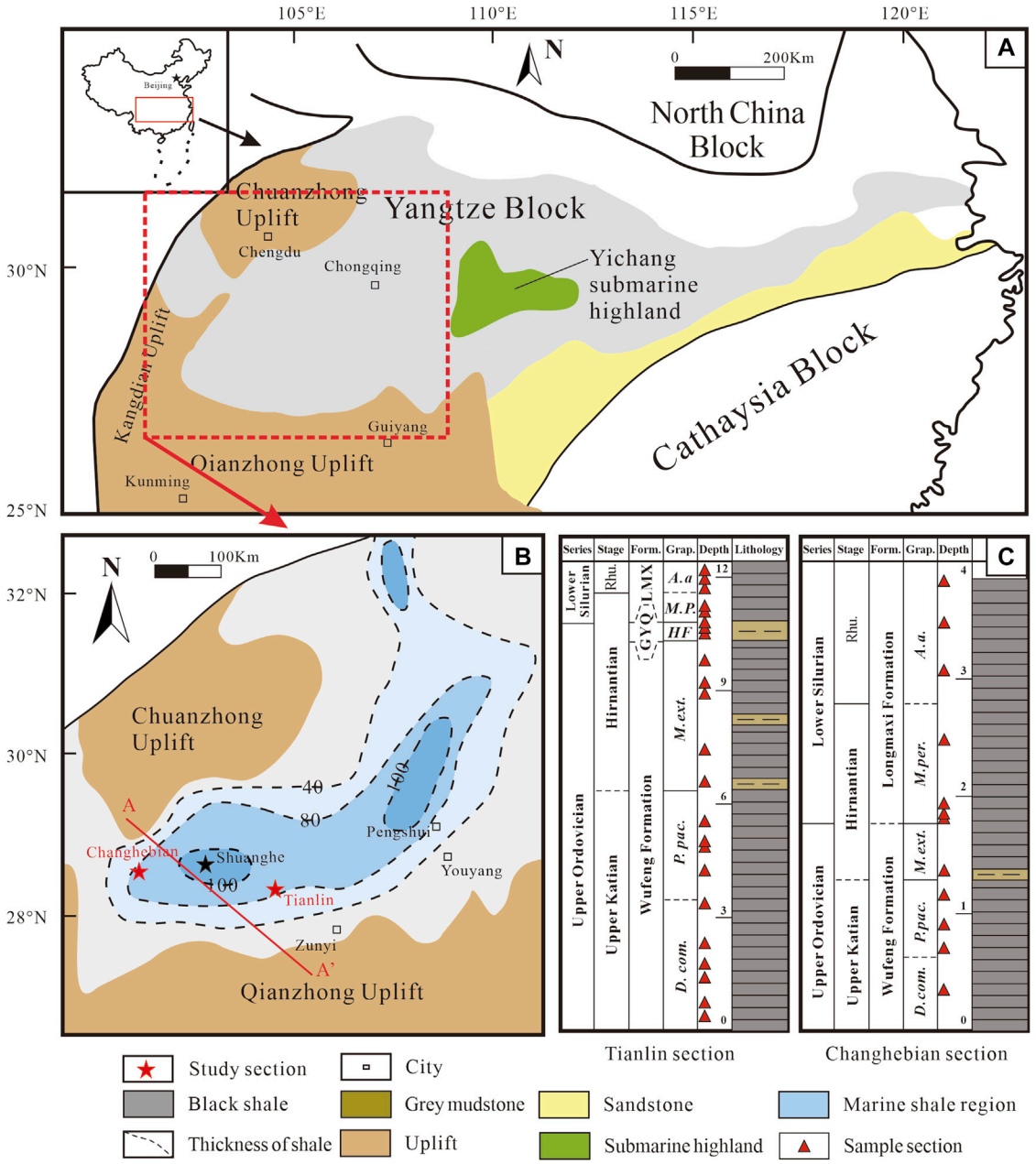

FIGURE 1 | (A) Paleogeographic map of the Upper Yangtze Basin (Chen et al., 2004). **(B)** Locations of the Tianlin, Changhebian, and Shuanghe sections (Liu et al., 2016). The dotted line in the figure shows the location of the eastern and southern depocenters within the Upper Yangtze Basin (Liang et al., 2009). Line A-A' represents the cross-section in **Figure 11**. **(C)** Comparison diagram of biostratigraphy in the study sections (graptolite biozones based on Chen et al. (2004)). GYQ, Guanyinqiao Formation; HF, Hirnantia Fauna; D. com, Dicellograptus complexus; P. pac, Paraorthograptus pacificus; M. ext., Metabolograptus extraordinarius; M.P., Metabolograptus persulptus; A. a., Akidograptus ascensus.

source area, respectively (Nesbitt and Young, 1982; Cullers and Podkovyrov, 2000) (Cox et al., 1995). The calculation formulas are as follows:

$$\mathrm{CIA} = \left[\mathrm{Al_2O_3}/\left(\mathrm{Al_2O_3} + \mathrm{CaO^*} + \mathrm{Na_2O} + \mathrm{K_2O}\right)\right] \times 100,$$

$$\mathrm{ICV} = \left(\mathrm{Fe_2O_3} + \mathrm{K_2O} + \mathrm{Na_2O} + \mathrm{CaO} + \mathrm{MgO} + \mathrm{MnO} + \mathrm{TiO_2}\right)/\mathrm{Al_2O_3}.$$

The principal concentration was calculated in moles. CaO* is the CaO in silicate, which can be calculated by the formula $\mathrm{CaO_{residual}}$ = mole CaO—10/3 × mole $\mathrm{P_2O_5}$ (McLennan, 2001). If $\mathrm{CaO_{residual}} < \mathrm{Na_2O}$, $\mathrm{CaO^*} = \mathrm{CaO_{residual}}$; otherwise, $\mathrm{CaO^*} = \mathrm{Na_2O}$. To eliminate the influence of potassium metasomatism on the CIA value, we used the alternative formula $\mathrm{CIA_{corr}} = [(1 - \mathrm{m})\ \mathrm{Al_2O_3}\ /\ (\mathrm{Al_2O_3} + \mathrm{CaO^*} + \mathrm{Na_2O} -$

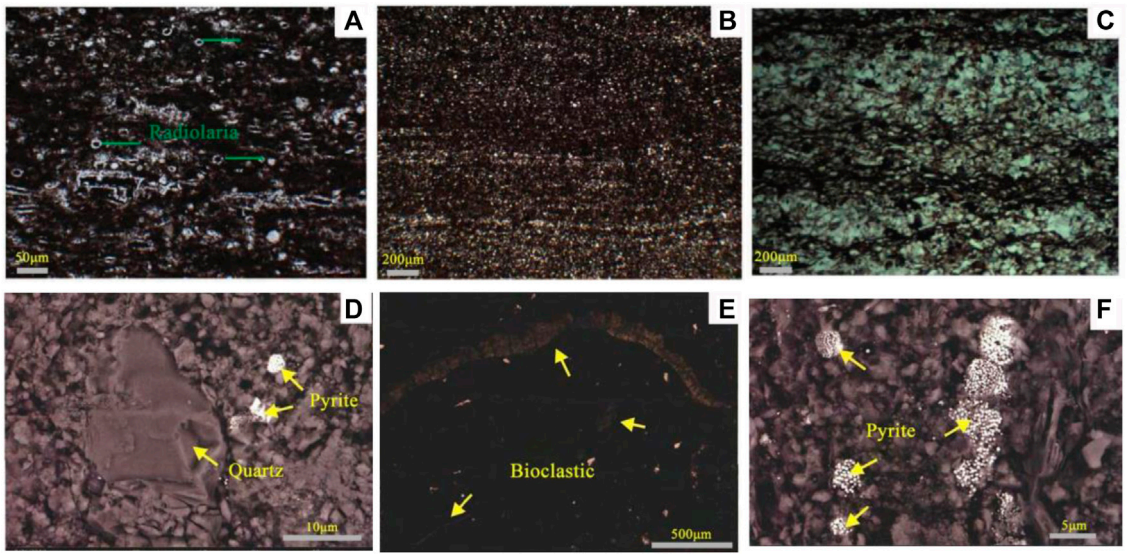

FIGURE 2 | (A) Radiolarian siliceous shale and **(B)** calcareous silt shale representing deep-water shelf facies and shallow shelf facies, respectively (Mou et al., 2016); **(C)** mud shale representing tidal-flat facies in the WF Formation from the Changhebian section; **(D)** quartz particles under a scanning electron microscope (SEM); **(E)** bioclastic fragments in the Guanyinqiao Formation (Mou et al., 2019); and **(F)** framboidal pyrite under the SEM.

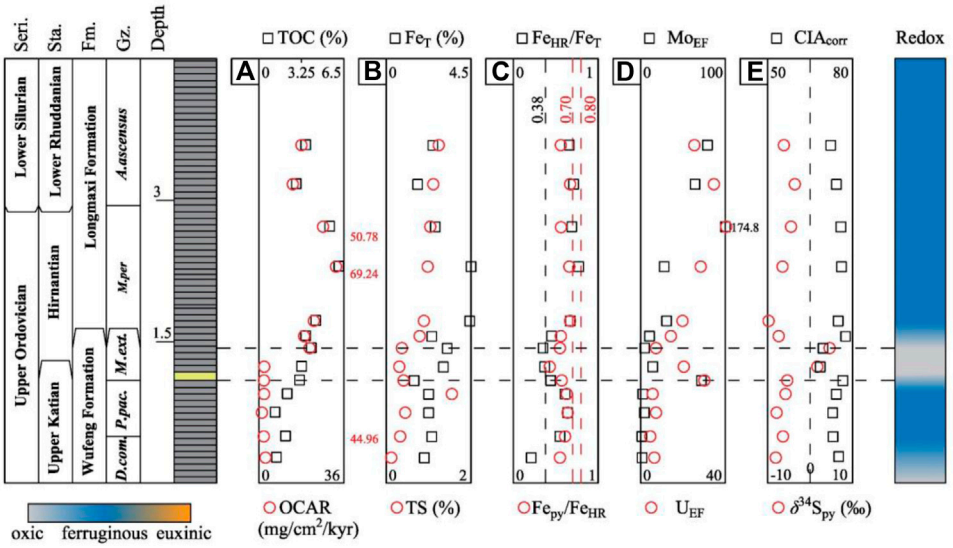

FIGURE 3 | Chemostratigraphic profiles of **(A)** TOC and OCAR, **(B)** Fe_T and TS, **(C)** Fe_{HR}/Fe_T and Fe_{py}/Fe_{HR}, **(D)** Mo_{EF} and U_{EF}, **(E)** CIA_{corr} and $\delta^{34}S_{py}$, and the redox summary for the Changhebian section. The vertical dotted line represents the threshold of each proxy. Abbreviations as in **Figure 1**.

$m^2Al_2O_3)] \times 100$, where $m = K_2O / (Al_2O_3 + CaO^* + Na_2O + K_2O)$ (Panahi et al., 2000).

By subtracting the contribution of the land source from the elemental content in the rock, the excess value of an element can represent its autogenic composition (Tribovillard et al., 2006; Algeo and Tribovillard, 2009). Therefore, a post-Archean average shale (PAAS) standardization analysis of the studied shale samples from the WF–LMX Formation was carried out to obtain the excess value of element X, and the formula is $X_{EF} = (X / Al)_{sample} / (X / Al)_{PAAS}$ (Taylor and McClcnnan, 1985). $X_{EF} > 1$ indicates its enrichment and vice versa.

The mass accumulation rate of organic carbon (OCAR) is one of the effective indicators for evaluating the marine primary productivity, the formula for which is OCAR = LSR×TOC×ρ, where LSR is the line sedimentation rate (m/Myr) and ρ means the density of rock (2.5 g/m^3) (Schoepfer et al., 2015) (The value of the LSR can be found in **Supplementary Table S1**).

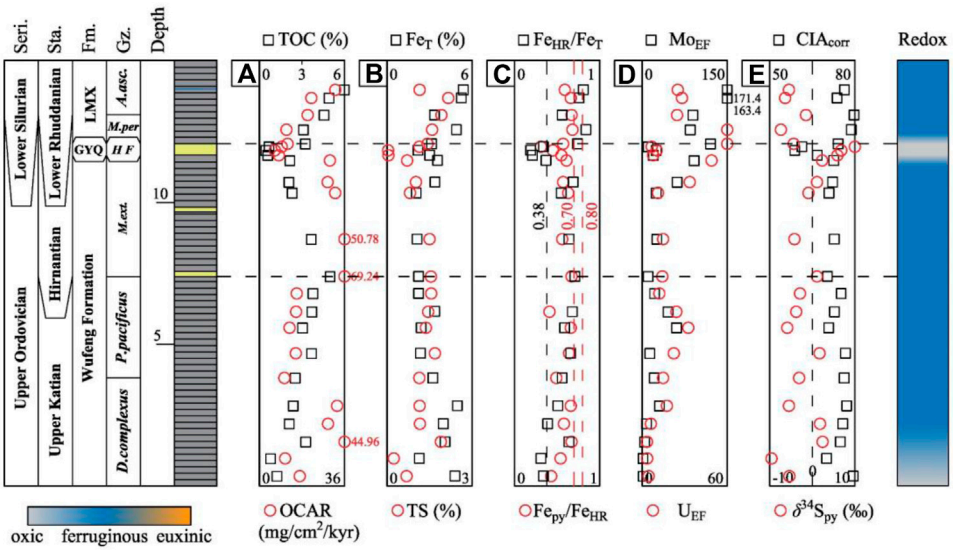

FIGURE 4 | Chemostratigraphic profiles of **(A)** TOC and OCAR, **(B)** Fe_T and TS, **(C)** Fe_{HR}/Fe_T and Fe_{py}/Fe_{HR}, **(D)** Mo_{EF} and U_{EF}, **(E)** CIA_{corr} and $\delta^{34}S_{py}$, and redox summary for the Tianlin section. The vertical dotted line represents the threshold of each proxy. Abbreviations as in **Figure 1**.

4 RESULTS

All petrological and geochemical data of the Tianlin and Changhebian sections are shown in **Tables 1**, **2** and **Supplementary Table S1**. The stratigraphic models of the key results are shown in **Figures 2–4**. The test data of the Shuanghe section can be found in Liu et al. (2016); Li et al. (2017); Liu et al. (2020); and Lu et al. (2021).

4.1 Petrological Characteristics

Field observation and microscopic studies showed that the shale samples of the WF–LMX Formations are mainly thin or massive, dark/black, and fine-grained (**Figure 2**), and include clay shale, calcium-rich clay shale, calcareous clay shale, siliceous clay shale, siliceous biogenic shale, and argillaceous siliceous shale (**Figures 2A–C**). Tidal-flat and shallow-water shelf facies were identified in the Changhebian section, and shallow and deep-water shelf facies were identified in the Tianlin section.

Under a polarizing microscope, the studied samples showed an argillaceous structure, composed of clay minerals and clastic particles (mainly quartz and feldspar), with a particle size of <0.0039 mm (**Figure 2D**). The clay minerals were parallelly oriented and alternated with black carbonaceous OM. Calcitic and dolomitic cements exist between the clay minerals as microcrystalline and rhombic crystals, respectively. Brachiopod fragments were observed in the gray-black calcium-bearing mudstone of the GYQ Formation (**Figure 2E**). Scanning electron microscope images showed fine euhedral to subhedral pyrite crystals, occurring as framboidal aggregates (**Figure 2F**).

4.2 Geochemical Characteristics

4.2.1 Total Organic Carbon and Total Sulfur Content

The variations in the TOC and total sulfur (TS) differed between the two sections. The Changhebian section showed a relatively high TOC content (1.24–6.11%, average 3.31%). It increased from the late Katian to the early Rhuddanian stage (**Table 1** and **Figure 3**). The TS content also showed an increasing trend, ranging from 0.12 to 1.55% (average 0.74%). TOC values in the Tianlin section were relatively low, ranging from 0.47 to 7.17% (average 2.89%). However, it showed an opposite trend compared with the Changhebian section with a trend of first decreasing and then increasing during the late Katian to the early Rhuddanian (**Table 1**; **Figure 4**). The TS content was relatively high, ranging from 0.04 to 2.85% (average 1.02%), and showed a trend similar to that of TOC (**Figure 4**).

4.2.2 Major and Trace Elements Content

The major element composition of the studied shales was similar in both sections, with high concentrations of SiO_2, Al_2O_3, CaO, Fe_2O_3, K_2O, and MgO, and relatively low (<1.0%) Na_2O, P_2O_5, TiO_2, and MnO concentrations (**Table 1**). For the Changhebian section, the averages of these major elements were 62.33, 10.74, 4.05, 3.82, 3.38, and 2.89%, respectively. For the Tianlin section, the averages of these major elements were 66.03, 10.86, 4.56, 3.18, 2.99, and 2.94%, respectively.

Variations in the trace element contents were estimated by calculating their enrichment factors (**Figure 5**). Compared with PAAS, both sections were enriched in Mo and U, marginally enriched in Th, Zr, Ba, La, and Ce, and depleted in Sc and Sr (**Table 2** and **Figure 5**).

TABLE 1 | Results of the TOC and major elements in the Changhebian and Tianlin sections.

Stage	Formation	Samples	Depth (m)	TOC (%)	Major element (wt, %)										ICV
					SiO_2	Al_2O_3	K_2O	Na_2O	Fe_2O_3	MgO	MnO	TiO_2	CaO	P_2O_5	
Changhebian section															
		CH-13	3.98	3.59	69.85	10.17	3.85	0.48	3.53	4.07	0.04	0.24	2.12	0.24	1.41
Rhuddanian		CH-12	3.52	2.86	67.11	9.17	2.03	0.65	2.37	3.54	0.03	0.12	2.44	0.05	1.24
	Longmaxi Formation	CH-11	3.02	5.42	72.79	9.93	2.01	0.71	3.71	2.77	0.04	0.21	1.17	0.06	1.07
Hirnantian		CH-10	2.55	6.11	71.76	10.06	3.15	0.56	6.44	0.52	0.06	0.19	3.18	0.12	1.15
		CH-09	1.91	4.35	53.36	11.11	3.89	0.37	6.33	4.16	0.06	0.31	3.49	0.28	1.68
		CH-08	1.73	3.58	60.44	12.37	4.44	0.41	3.44	4.12	0.03	0.49	3.33	0.11	1.36
		CH-07	1.59	4.01	58.44	7.11	3.88	0.11	4.61	1.13	0.02	0.11	3.88	0.41	1.73
		CH-06	1.37	3.27	59.17	10.35	3.87	0.85	4.33	4.15	0.03	0.33	3.11	0.46	1.61
		CH-05	1.21	3.11	62.11	11.03	4.33	0.65	2.11	2.11	0.02	0.44	4.12	0.46	1.08
	Wufeng Formation	CH-04	1.05	2.17	61.88	14.01	4.55	0.64	3.22	2.48	0.03	0.68	7.15	0.44	1.34
		CH-03	0.83	1.24	64.31	11.77	2.11	0.88	3.21	2.44	0.03	0.39	4.89	0.74	1.27
Late Katian		CH-02	0.55	2.03	59.11	12.34	4.11	0.65	3.44	3.07	0.02	0.48	8.99	1.56	1.68
		CH-01	0.30	1.34	49.94	10.16	3.14	0.44	2.88	2.98	0.02	0.22	7.45	1.07	1.69
Tianlin section															
		TL-23	12.10	7.17	72.12	7.69	1.58	0.51	5.11	2.14	0.08	0.37	1.77	0.15	1.50
Rhuddanian		TL-22	11.85	4.91	70.23	10.25	2.37	0.81	4.98	3.61	0.07	0.5	1.88	0.21	1.39
	Longmaxi Formation	TL-21	11.33	4.56	69.98	11.55	3.15	0.21	3.19	3.31	0.05	0.57	1.79	0.33	1.06
		TL-20	10.88	3.11	70.76	10.75	3.44	0.13	4.65	3.19	0.07	0.54	1.28	0.25	1.24
		TL-19	10.45	3.24	64.31	9.88	4.07	0.24	2.98	3.56	0.04	0.5	1.96	0.38	1.35
		TL-18	10.36	0.68	60.34	13.22	2.01	3.22	2.54	2.11	0.01	0.62	9.87	0.08	1.54
		TL-17	10.25	0.47	55.33	12.55	3.12	2.98	2.07	1.03	0.01	0.58	10.07	0.42	1.58
	GYQ Formation	TL-16	10.10	0.59	52.44	14.44	3.11	2.21	2.85	2.93	0.02	0.67	13.22	0.08	1.73
Hirnantian		TL-15	9.94	2.15	55.38	12.43	3.22	0.99	3.38	3.3	0.04	0.58	11.37	0.83	1.84
		TL-14	9.28	2.08	61.21	12.93	3.46	1.04	3.21	3.37	0.03	0.62	3.34	0.47	1.17
		TL-13	8.95	2.31	77.16	7.19	3.65	0.21	1.95	0.77	0.02	0.35	0.45	0.06	1.03
		TL-12	7.54	3.66	75.03	7.83	2.84	0.37	2.01	1.88	0.02	0.38	1.75	0.27	1.18
		TL-11	6.40	4.99	72.13	9.62	2.66	1.11	2.11	2.32	0.02	0.37	1.11	0.12	1.01
		TL-10	5.88	3.78	70.33	11.02	2.48	0.76	2.12	3.33	0.02	0.55	1.76	0.21	1.00
		TL-05	5.32	3.71	68.69	10.4	2.45	0.89	3.22	2.04	0.03	0.51	4.89	0.23	1.35
	Wufeng Formation	TL-05	4.83	3.05	71.64	9.38	2.11	1.07	2.29	2.11	0.02	0.45	1.56	0.18	1.02
		TL-05	4.05	3.68	79.88	7.61	2.05	0.32	2.24	2.11	0.02	0.36	1.77	0.09	1.17
Late Katian		TL-05	3.30	2.53	71.53	9.65	2.94	0.34	3.07	3.12	0.03	0.44	4.98	0.2	1.55
		TL-05	2.45	2.39	64.53	13.33	3.8	0.45	4.71	3.54	0.04	0.64	7.29	0.99	1.54
		TL-04	1.90	2.11	59.97	11.33	3.11	0.54	3.77	2.89	0.03	0.56	4.89	0.44	1.39
		TL-03	1.35	3.27	58.35	15.44	4.72	0.7	3.89	5.15	0.03	0.71	6.96	0.08	1.44
		TL-02	0.84	0.79	65.41	8.77	3.88	0.44	2.15	3.15	0.02	0.41	3.14	0.12	1.50
		TL-01	0.30	1.24	51.89	12.52	2.44	0.57	4.55	6.71	0.03	0.59	7.85	0.07	1.82

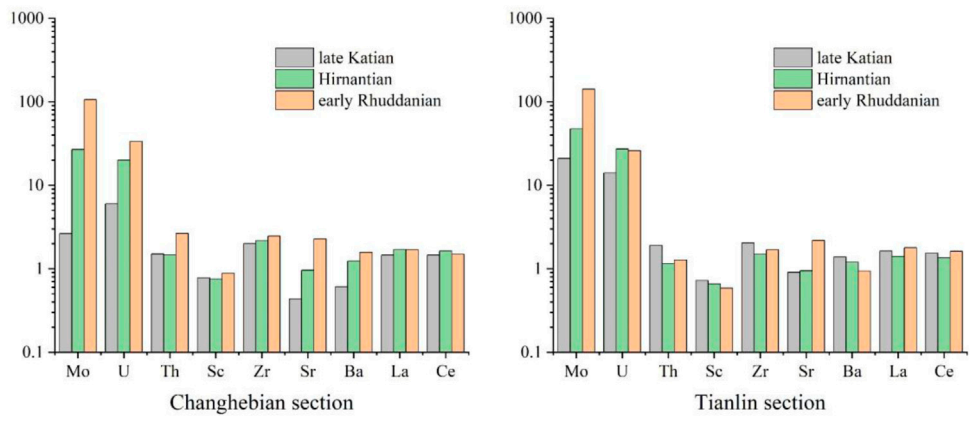

FIGURE 5 | Enrichment of trace elements in the Changhebian and Tianlin sections.

TABLE 2 | Results of trace elements and $\delta^{34}S_{py}$ in the Changhebian and Tianlin sections.

Stage	Formation	Samples	Depth (m)	$\delta^{34}S_{py}$ (‰)	Trace elements (ppm)								
					Mo	U	Th	Sc	Zr	Sr	Ba	La	Ce
Changhebian section													
	Longmaxi	CH-13	3.98	–6.2	50.6	14.6	25	10	330	354	684	41.79	74.64
Rhuddanian	Formation	CH-12	3.52	–3.6	37.2	18.2	24	9	315	255	511	39.78	77.99
		CH-11	3.02	–4.5	109.4	23.0	22	7	308	233	699	36.44	66.92
Hirnantian		CH-10	2.55	–6.5	17.7	16.4	23	9	396	254	896	34.83	76.32
		CH-09	1.91	–9.8	21.5	12.6	15	10	410	174	851	29.96	61.03
		CH-08	1.73	–7.4	8.2	10.1	12	5	231	77	489	31.45	61.20
		CH-07	1.59	4.6	2.2	3.0	8	6	216	84	437	50.33	99.43
	Wufeng Formation	CH-06	1.37	1.7	9.4	12.1	15	9	288	47	325	52.17	102.29
		CH-05	1.21	–5.4	50.0	19.0	10	7	217	98	458	39.07	82.16
Late Katian		CH-04	1.05	–5.8	2.3	4.6	5	3	133	77	298	44.15	96.75
		CH-03	0.83	–7.9	3.3	4.9	21	10	310	83	345	39.96	80.78
		CH-02	0.55	–6.4	1.2	3.3	23	12	396	74	338	47.69	100.29
		CH-01	0.30	–8.1	1.2	3.8	15	11	385	34	217	34.98	74.77
Tianlin section													
	Longmaxi	TL-23	12.10	–5.5	83.1	11.1	17	3	264	328	630	36.94	67.46
Rhuddanian	Formation	TL-22	11.85	–6.4	105.6	16.5	17	7	245	112	175	33.94	71.60
		TL-21	11.33	–1.5	65.3	16.3	16	8	261	334	822	54.33	100.05
Hirnantian		TL-20	10.88	–7.4	57.5	38.0	12	8	192	141	278	38.99	76.22
		TL-19	10.45	–4.4	75.2	35.0	18	7	357	234	886	37.69	89.75
	GYQ Formation	TL-18	10.36	11.7	8.7	5.1	10	7	168	62	334	46.33	98.22
		TL-17	10.25	6.8	19.6	7.3	9	6	162	51	469	34.56	74.29
		TL-16	10.10	5.9	17.9	6.4	9	6	138	35	311	37.82	76.87
	Wufeng Formation	TL-15	9.94	2.3	71.9	34.9	6	4	125	77	448	41.82	88.59
		TL-14	9.28	1.1	50.4	24.8	8	5	171	69	355	38.46	75.58
		TL-13	8.95	–0.9	11.2	4.6	14	9	234	113	409	26.44	46.84
		TL-12	7.54	–4.2	12.7	6.6	14	9	243	242	1108	29.19	57.66
		TL-11	6.40	1.1	6.4	7.9	7	6	210	121	297	33.14	60.81
Late Katian		TL-10	5.88	–2.9	15.3	7.6	9	6	196	128	357	45.88	100.54
		TL-05	5.32	–3.8	30.1	14.4	7	4	147	126	337	35.54	80.59
		TL-05	4.83	–5.9	35.9	17.5	10	6	184	200	916	35.41	69.65
		TL-05	4.05	1.7	6.5	9.7	9	6	192	95	369	28.24	47.88
		TL-05	3.30	–3.1	13.0	8.1	11	7	182	122	377	43.55	79.97
		TL-05	2.45	–5.5	25.6	13.3	14	9	260	165	544	74.16	134.26
		TL-04	1.90	1.8	5.5	4.0	20	13	364	121	368	35.69	75.66
		TL-03	1.35	2.4	4.4	2.9	14	8	297	88	248	40.39	70.92
		TL-02	0.84	–9.6	0.9	1.8	17	10	288	95	211	43.33	84.32
		TL-01	0.30	–5.4	1.3	3.2	14	9	299	56	246	39.54	89.66

4.2.3 Variations of the $\delta^{34}S_{py}$

The $\delta^{34}S_{py}$ contents of these two sections had similar characteristics. They increased from the late Katian to the Hirnantian, followed by a decrease in the early Rhuddanian (**Figures 3**, **4**). In addition, the average $\delta^{34}S_{py}$ content in the Changhebian section (−5.02‰) was lower than that in the Tianlin section (−1.37‰) (**Table 2**).

5 DISCUSSION

5.1 Sediment Provenance and Paleoweathering

The geochemical characteristics (major and trace elements) of fine clastic sedimentary rocks are indicators of source material compositions and tectonic environments, and provide information on the tectonic evolution of an area (Hofmann, 2005; Sugitani et al., 2006; Liu et al., 2007; Cottle et al., 2009; Cawood et al., 2012; Zaid, 2015; Zhang et al., 2018).

Based on the different stabilities of Zr, Th, and Sc in sedimentary cycles, their ratios can be used to determine whether the source rocks were a part of the sedimentary cycles (Cullers and Podkovyrov, 2000; McLennan, 2001). Generally, unrecycled sediments follow the magmatic evolution trend in the cross-plots of Th/Sc and Zr/Sc, whereas the recycled sediments follow the trend of zircon addition because of its continuous enrichment (**Figure 6A**). The studied samples followed the magmatic evolution array and were closer to more felsic end-members, indicating that the source rocks were unrecycled and felsic (**Figure 6A**). The TiO_2–Zr cross-plot can also be used to determine the source rock composition, with values of <55 and >195 representing felsic and mafic rocks, respectively (Hayashi et al., 1997). In this work, all shale samples were located in the area of felsic igneous rocks, which is consistent with the results obtained by Th/Sc-Zr/Sc, indicating that the source was mainly felsic (**Figure 6B**).

The depositional environment of the basin not only controls the thickness, area, OM type, and maturity of sedimentary shale

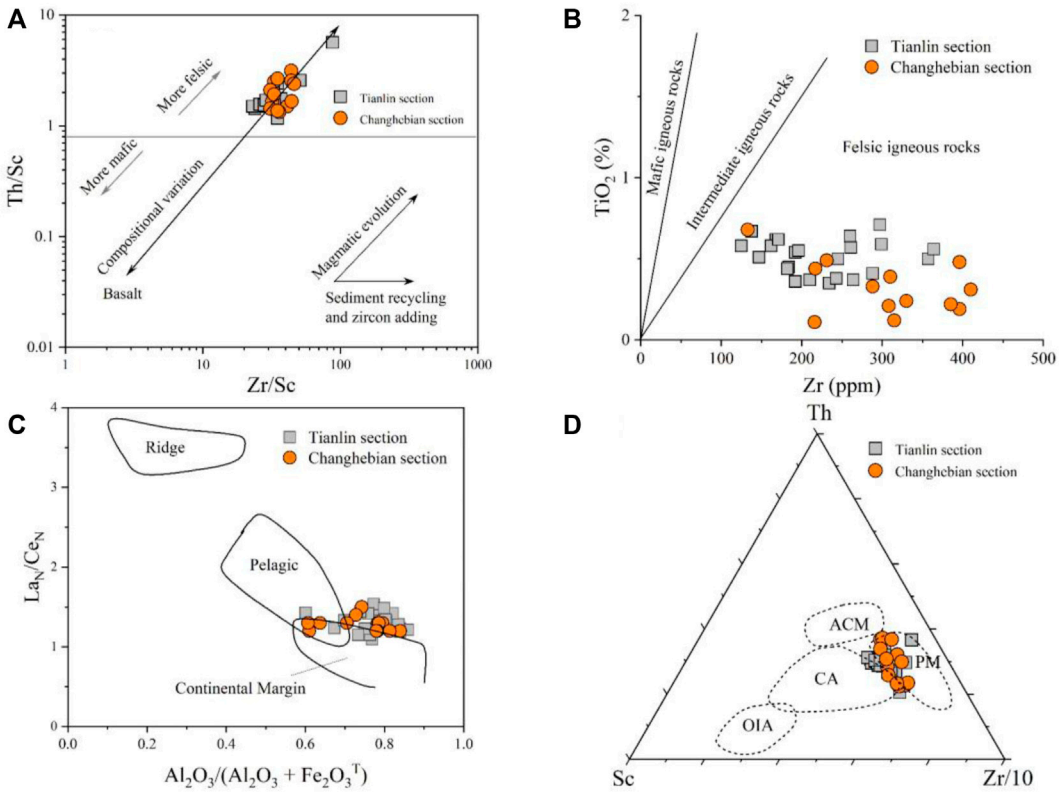

FIGURE 6 | Sedimentary provenance for the Changhebian and Tianlin sections: **(A)** Zr/Sc versus Th/Sc, **(B)** Zr versus TiO_2, **(C)** $Al_2O_3/(Al_2O_3+Fe_2O_3)$ versus La_N/Ce_N, and **(D)** Th-Sc-Ze/10 ternary diagram. CA, continental island arc; ACM, active continental margin; OIA, oceanic island arc; PM, passive margin.

but it also affects the type and mineral composition of the sedimentary rocks (McLennan, 2001). Based on their variable Ce anomalies, the sedimentary environment can be classified into expanding ridge, pelagic, and continental margins (Murray, 1994). The $Al_2O_3/(Al_2O_3+Fe_2O_3)$-$La_N/Ce_N$ intersection diagram suggests a continental margin environment for the studied samples (**Figure 6C**) (Murray, 1994). In addition, depending on the tectonic setting, the sedimentary basin can be divided into the active continental margin, oceanic island arc, continental island arc, and passive continental margin (PM), which can be identified from the Th-Sc-Zr/10 ternary plot (Bhatia and Crook, 1986). The samples from the Changhebian and Tianlin sections were located in or near the PM field, which further supports that the sedimentary environment was a passive margin (**Figure 6D**).

Before determining the paleoclimate and its intensity, it is necessary to determine whether the provenance of the parent rock was affected by sedimentary differentiation and recycling. The ICV is usually used to determine whether the source rock composition is a primary deposition (ICV>1) or recycled sediment (ICV<1) (Cullers and Podkovyrov, 2000, 2002). The ICV values of the studied shale samples were >1 (**Table 1**), suggesting immature deposits. The CIA value can be used to estimate the degree of weathering of the source area (Cox et al., 1995). From the vertical variation trend of CIA, we infer that the Changhebian and Tianlin sections experienced similar weathering intensities during the O–S period (**Figures 3**, **4**). The sections experienced moderate weathering in the late Katian stage (CIA = 75), and relatively weak weathering in the Hirnantian stage (CIA = 72 for the Changhebian section and CIA = 70 for the Tianlin section). Weathering conditions gradually became moderate in the early Rhuddanian stage (CIA = 74 for the Changhebian section, and CIA = 77 for the Tianlin section) (**Figures 3**, **4**; **Supplementary Table S1**).

5.2 Water Restriction

The degree of restriction of the water column affects the enrichment and preservation of sedimentary OM and limits the biogeochemical cycle of elements (Algeo and Rowe, 2012). Mo and U show different adsorption rates and trends in restricted and unrestricted environments, and the covariant relationship between U_{EF} and Mo_{EF} is often used to determine the restriction degree of the water column and the local depositional environment (Algeo and Tribovillard, 2009; Tribovillard et al., 2012).

The degree of water restriction showed a similar trend for both sections during the O–S period. From the late Katian to the Hirnantian, the EF of Mo and U in shale samples gradually increased, thereby increasing the Mo_{EF}/U_{EF} ratio from 0.1×SW to 0.3×SW (**Figures 7A,B**). In addition, the reducibility of the water column gradually increased from suboxic to anoxic conditions (**Figures 7A,B**), which continued during the Hirnantian to the

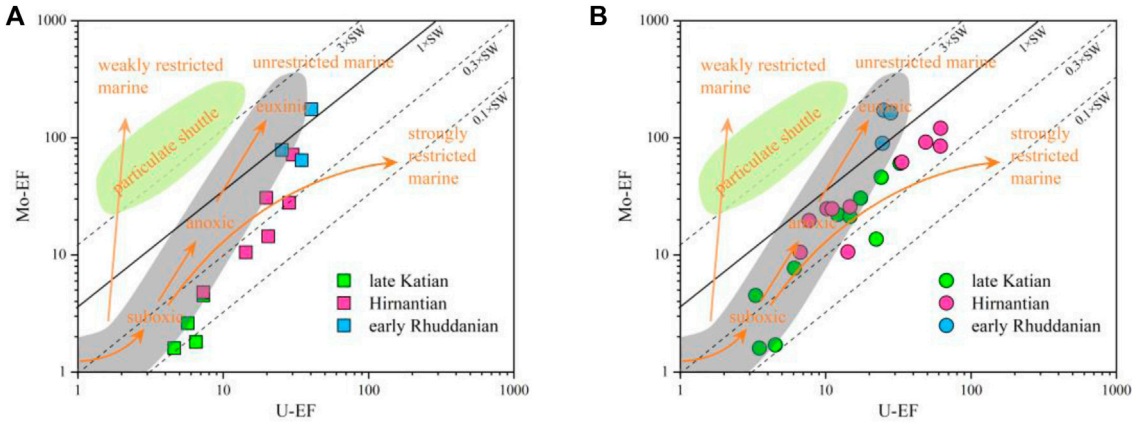

FIGURE 7 | Covariant relationship between U_{EF} and Mo_{EF} for the **(A)** Changhebian section and **(B)** Tianlin section. The solid line represents the molar concentration ratio of Mo/U in seawater (SW = 7.9).

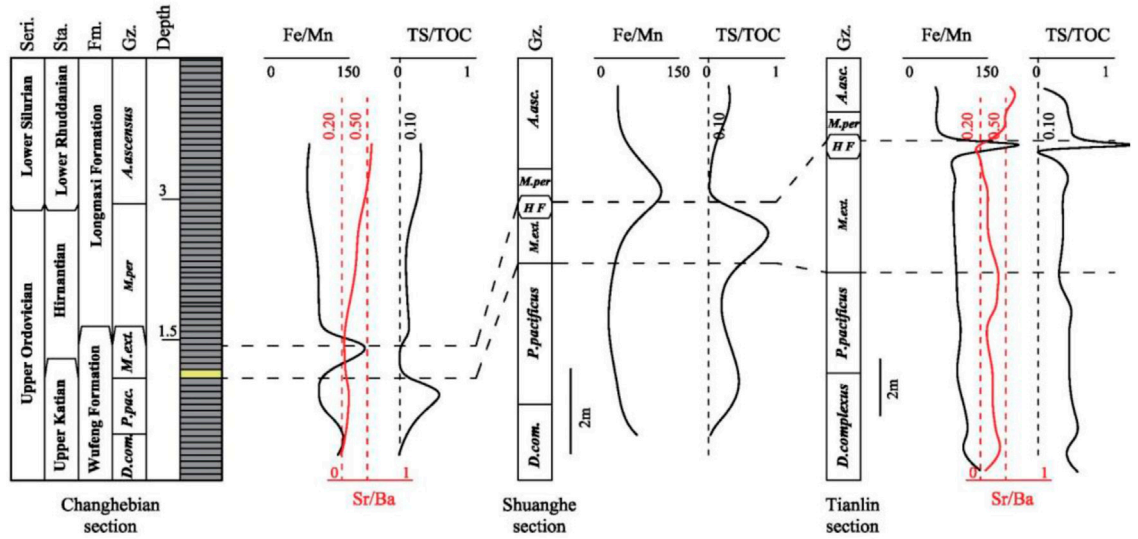

FIGURE 8 | Comparison of paleo-water depth and paleosalinity for the study sections. The data on the Shuanghe section are from Li et al. (2017). Abbreviations as in **Figure 1**. Red and black vertical dashed lines represent thresholds for proxies, as shown in the text.

early Rhuddanian stage, and reached euxinic conditions (Mo_{EF}/U_{EF} = ~1×SW). This feature is similar to the variation pattern of Mo–U in the Black Sea, which represents a strongly restricted water environment.

In addition, the water column of the Changhebian section was more restrictive than that of the Tianlin section (**Figures 7A,B**), which may be related to the different paleowater depths and locations of the section during this period. The deeper the paleowater depth, the stronger the reduction of the water column will be, and the higher values of the Mo_{EF} and U_{EF}. Under the influence of the ocean current, the Tianlin section located on the east bank of the paleo-uplift (paleomagnetic direction) receives more Mo and U supplies than that of the Changhebian section, showing a relatively weak water restriction.

5.3 Paleowater Depth and Paleosalinity

The paleo-water depth determines the hydrodynamic and redox conditions, paleosalinity and paleoproductivity of sediment formation, and is an important indicator for the restoration and study of the sedimentary paleo-environment (Wang et al., 2020). In-depth research methods for the quantitative restoration of paleo-water depth in marine fine-grained sediments are not available. In this study, the value of Fe/Mn was used to characterize the variation trend of paleo-water depth in the study area during the O–S period, where a higher ratio was attributed to a water column (Wersin et al., 1991; Katz and Lin, 2014). This is because, during the Fe–Mn migration, Fe is easily oxidized to precipitate, whereas Mn is relatively stable and can be transported to deep-water areas far from the coast.

From the late Katian to the Hirnantian stage, and then to the early Rhuddanian stage, the paleo-water depth of the Changhebian and Tianlin sections had a similar change trend: shallow-deep-shallow-deep (**Figure 8**). Considering the Fe/Mn values of the Shuanghe section, the distribution of the paleo-water depth from deep to shallow was in the order of Shuanghe section (average 57.4) > Tianlin section (average 102.7) > Changhebian section (average 111.1) (**Supplementary Table S1**). This inference is consistent with the observed lithofacies characteristics representing the different water depths (see **Section 4.1**).

Paleosalinity is also an important indicator of the paleoenvironment and paleoecology and affects the enrichment of sedimentary OM (Arz et al., 2003; Hu et al., 2018). Paleosalinity also indirectly reflects the influence of coastal rivers on the sedimentary area, where a lower salinity denotes a stronger freshwater supply, and higher input of terrigenous clastic materials, and vice versa (Arz et al., 2003). Here, we used strontium/barium (Sr/Ba) and total sulfur/total organic carbon (S/TOC) ratios to restore the paleosalinity of the O–S period in the study area (Wei and Algeo, 2020). The values of Sr/Ba are <0.2 in fresh water, 0.2–0.5 in brackish, and >0.5 in seawater. The values of S/TOC are <0.1 in fresh water, >0.1 in brackish, and seawater (Wei and Algeo, 2020).

From the late Katian to the early Rhuddanian stage, the paleosalinity in the Changhebian and Tianlin sections first decreased and then increased (**Figure 8**). Specifically, the water column of the Changhebian section was brackish (Sr/Ba = 0.22, TS/TOC = 0.33) during the late Katian period, and in the transition zone from fresh water to brackish (Sr/Ba = 0.20, TS/TOC = 0.15) during the Hirnantian period. In the early Rhuddanian period, it returned to brackish conditions (Sr/Ba = 0.45, TS/TOC = 0.31). For the Tianlin section, the water column was brackish (Sr/Ba = 0.32, TS/TOC = 0.34), brackish (Sr/Ba = 0.24, TS/TOC = 0.28), and seawater (Sr/Ba = 0.52, S/TOC = 0.36) in the aforementioned three stages, respectively. The paleosalinity of the water column in the Tianlin section was greater than that in the Changhebian section, which was similar to the change in the paleo-water depth. (**Figure 8**). For the Shuanghe section, the water column was brackish and seawater during the O–S period, and its salinity showed an increasing trend during the Hirnantian stage, which may be related to the fall in sea level and increase in water restriction during this stage (see **section 5.5** for a specific discussion).

5.4 Redox Conditions and its Heterogeneity

5.4.1 Reconstruction of Redox Conditions

Fe speciation and its ratio has been widely used to determine the redox conditions in sedimentary water columns (Poulton and Canfield, 2011; Li et al., 2015; Jin et al., 2016). Under Fe_T > 0.5%, the ratio of highly active iron (Fe_{HR}) to total iron (Fe_T) is used to distinguish oxic conditions (Fe_{HR}/Fe_T < 0.38) and anoxic conditions (Fe_{HR}/Fe_T > 0.38). Furthermore, under anoxic conditions, the ratio of pyrite (Fe_{py}) to Fe_{HR} is used to distinguish between ferruginous (Fe_{py}/Fe_{HR} < 0.7–0.8) and euxinic (Fe_{py}/Fe_{HR} > 0.7–0.8) conditions (Poulton and Canfield, 2011; Clarkson et al., 2014). The Fe_T values of the 36 studied samples were all ≥ 0.5%, which could be used to determine the redox conditions of the water column (**Supplementary Table S1**). In addition, we used the U_{EF}-Mo_{EF} covariance diagram to further infer the redox conditions of the water column.

In the Changhebian section, during the late Katian stage (from the *D. complexus* zone to the *P. pacificus* zone), the redox conditions of the water column changed from oxic-suboxic (Fe_{HR}/Fe_T = 0.21) to anoxic conditions (Fe_{HR}/Fe_T = 0.60), especially ferruginous (Fe_{py}/Fe_{HR} = 0.62). During the early Hirnantian stage (*M. extraordinarius*), the water conditions gradually leaned toward suboxic (Fe_{HR}/Fe_T = 0.38), but in the late Hirnantian, they returned to ferruginous (Fe_{HR}/Fe_T = 0.56, Fe_{py}/Fe_{HR} = 0.61), and these conditions lasted until the early Rhuddanian stage (**Supplementary Table S1** and **Figure 9**).

In the Tianlin section, in the early late Katian stage (*D. complexus* zone), the redox conditions of the water column changed from oxic-suboxic (Fe_{HR}/Fe_T = 0.33) to anoxic (Fe_{HR}/Fe_T = 0.51), especially ferruginous (Fe_{py}/Fe_{HR} = 0.64), which lasted for the middle Hirnantian stage (before the GYQ Formation in the *Hirnantia Fauna* zone). During the deposition of the GYQ Formation, the water column gradually changed to suboxic (Fe_{HR}/Fe_T = 0.25), then returned to a ferruginous condition (Fe_{HR}/Fe_T = 0.79, Fe_{py}/Fe_{HR} = 0.63) in the late Hirnantian (*M. persulptus* zone), and lasted until the early Rhuddanian stage (Fe_{HR}/Fe_T = 0.71, Fe_{py}/Fe_{HR} = 0.64).

In summary, the Changhebian and Tianlin sections accumulated under oxic-suboxic conditions during the early late Katian (early *D. complexus* zone) and the middle Hirnantian (*Hirnantia Faun*), but shifted to anoxic conditions (especially ferruginous) during the other stage. This change is consistent with the results of the Mo_{EF}-U_{EF} plot (**Figure 7**, **Section 5.2**).

5.4.2 Redox Heterogeneity in the Southwest Depocenter

To confirm the heterogeneous redox conditions in the Upper Yangtze Basin, we compared and discussed the values of Fe_{HR}/Fe_T and Fe_{py}/Fe_{HR} from the Changhebian and Tianlin sections with those of the Shuanghe section [**Figure 9** (Liu et al., 2016)]. In the early late Katian, the marine water column of the Changhebian and Tianlin sections (located in the nearshore area) maintained oxic-dysoxic conditions, whereas the Shuanghe section (located in the offshore area) showed ferruginous conditions, which confirms the deepest paleo-water of the Shuanghe section. During the early Hirnantian stage, ferruginous conditions in the basin expanded further, covering almost the entire southwest depocenter of the Upper Yangtze Basin. During the Hirnantian stage, under the influence of glaciation, the redox condition of the water column in the nearshore area gradually changed to oxic-dysoxic, while the reducibility of the anoxic condition in the Shuanghe section was further enhanced, with the appearance of the euxinic condition (**Figure 9**) (Liu et al., 2016; Li et al., 2019). In the late Hirnantian to the early Rhuddanian stage, the ferruginous condition of the water column was re-established in the southwest depocenter.

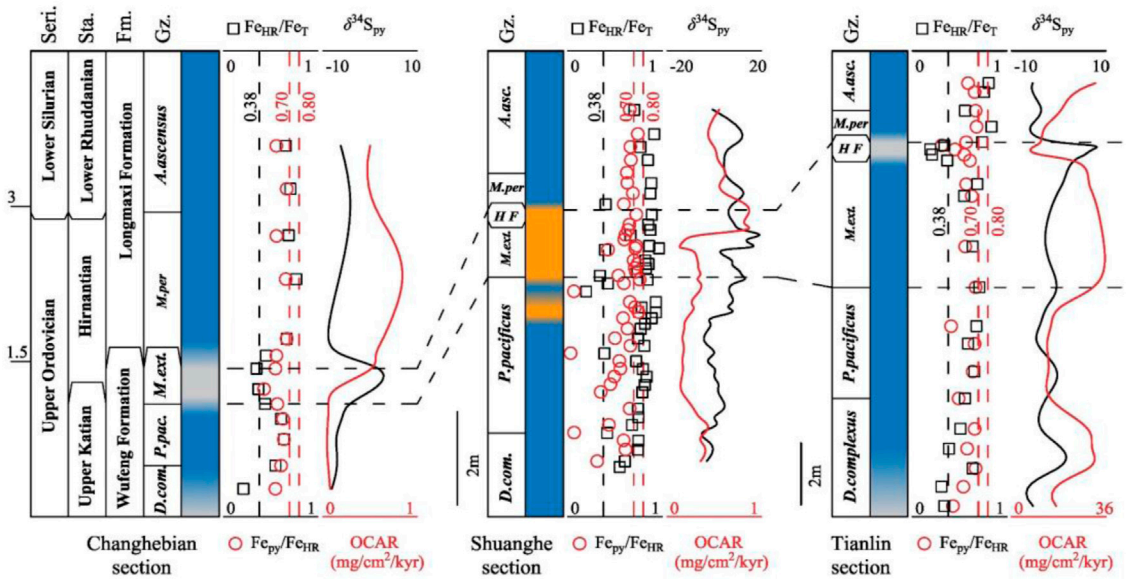

FIGURE 9 | Comparison of the redox condition, $\delta^{34}S_{py}$, and OCAR for the three sections. The data of the Shuanghe section are from Liu et al. (2016) and Li et al. (2017). Red and black vertical dashed lines represent thresholds for proxies, as shown in the text.

5.5 Control Factors of the Marine Redox Condition

Under a similar tectonic background and water restriction, the redox conditions of the water column in the southwest depocenter of the Upper Yangtze Basin still showed prominent spatiotemporal heterogeneity. Especially during the Hirnantian stage, euxinic appeared offshore when oxic-suboxic conditions appeared in the nearshore.

The mechanism of the formation of the euxinic condition has been widely studied: under anoxic conditions, microorganisms breathe by reducing sulfate to produce H_2S, which is combined with Fe_{HR} in water to form pyrite in a ratio of 2:1. When Fe_{HR} is depleted, H_2S accumulates in the water column and it finally forms the euxinic condition. Therefore, the effectiveness of sulfate and the input of Fe_{HR} jointly control euxinic acid production (Johnston et al., 2010; Raiswell and Canfield, 2012). In addition, under the influence of a limited sulfate supply, the S isotope value of sulfide generated by the microbial reduction of sulfate increases, resulting in a positive deviation of $\delta^{34}S_{py}$ (Leavitt et al., 2013; Bradley et al., 2016).

In this study, we classified the late Katian and early Rhuddanian stages into pre-glacial and postglacial periods, with the Hirnantian stage as the boundary, to explore the control factors of water redox conditions in the southwest depocenter of the Upper Yangtze Basin during the O–S period.

5.5.1 Pre-glacial and Postglacial Periods

During most of the pre-glacial and postglacial periods, the southwest depocenter of the Upper Yangtze Basin was in an anoxic ferruginous condition (**Figure 9**). The prevalence of ferruginous conditions is related to sufficient Fe_{HR} input and limited sulfate supply, and under high availability of OM and anoxic conditions, H_2S, which is produced by microorganisms, is eliminated by Fe_{HR} (Poulton and Canfield, 2011). For the Changhebian and Tianlin sections, the Fe_U values of the samples measured under the ferruginous conditions were higher (0.48–1.60%, average: 0.93% for the Changhebian section, and 0.46–2.11%, average 1.01% for the Tianlin section, **Supplementary Table S1**), suggesting a large input from terrestrial clay minerals and other silicates providing abundant detrital Fe flux. However, the Fe_U values of the samples were relatively small (Fe_U < 0.4%, **Supplementary Table S1**) in the Shuanghe section under the same ferruginous conditions, representing a limited detrital Fe flux. The input difference of Fe_U is also reflected in Fe_T. The highest value of Fe_T is observed in the Tianlin section (1.48–3.58%, average: 2.44%), followed by the Changhebian section (1.66–2.60%, average: 2.24%), and the Shuanghe section (0.60–3.00%, average: 1.33%).

Although the availability of OM was a major factor in controlling the redox conditions of the water column, especially for the development of the euxinic environment, euxinic conditions did not occur in the study area during this period (**Figure 9**). In addition, there was no significant positive correlation between OCAR and Fe_{py}/Fe_{HR} in the Changhebian ($r = 0.25$, $p > 0.10$) and Tianlin ($r = 0.30$, $p > 0.10$) sections (**Figure 10A**). Especially in the Shuanghe section, a ferruginous condition was still developed under low Fe_T input and high OCAR (18.30–45.00, average: 30.11 mg cm^{-2} myr^{-1}) (**Supplementary Table S1**, **Figure 9**), probably because of the effectiveness of sulfate.

Under moderate to strong hydrological restriction, when terrigenous clastic sulfate is input from the uplift to the depocenter, the sulfate concentration is high in the near-source region (i.e., the estuary), and low in the far-source region (i.e., the

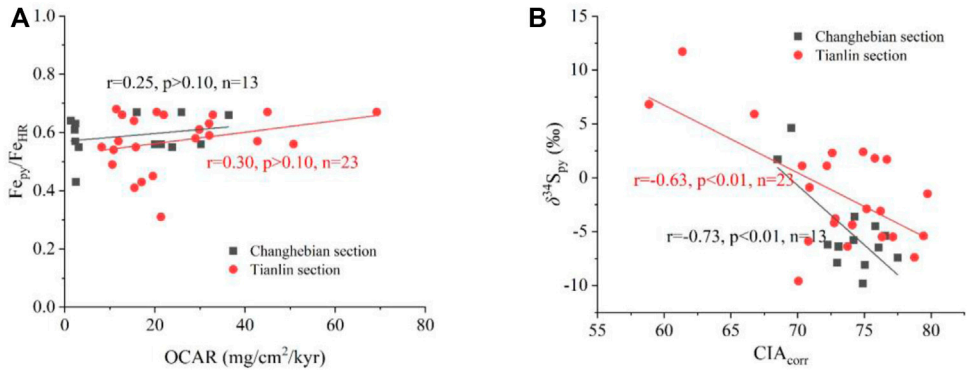

FIGURE 10 | Relationship between **(A)** OCAR and Fe_{py}/Fe_{HR}, **(B)** CIA_{corr} and $\delta^{34}S_{py}$.

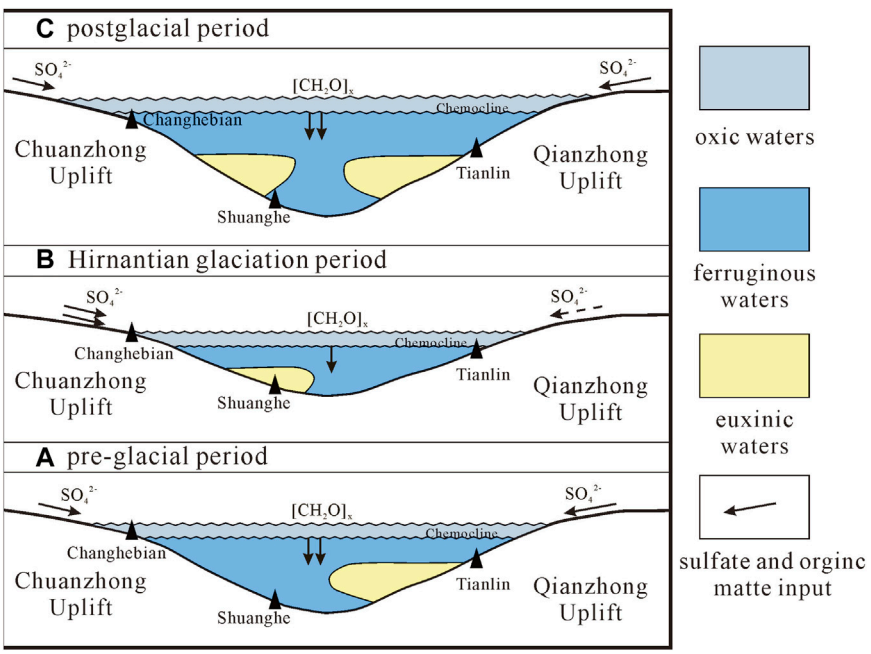

FIGURE 11 | Depositional model of A-A' (**Figure 1C**) during the Late Ordovician to Early Silurian. **(A)** Pre-glacial period; **(B)** Hirnantian glaciation period; and **(C)** postglacial period in the southwest depocenter of the Upper Yangtze Basin.

sedimentary center) (Li et al., 2019). The closer it is to the estuary, the lower will be the $\delta^{34}S$ value of the sulfide generated in the water column. This conclusion is supported by the significant negative relationships between $\delta^{34}S_{py}$ and CIA_{corr} ($r = -0.73$ for the Changhebian section, and $r = -0.63$ for the Tianlin section, with $p < 0.01$) (**Figure 10B**). During the pre-glacial and postglacial periods, the $\delta^{34}S_{py}$ value was the lowest in the Changhebian section (−7.05‰ for the late Katian, and −4.8‰ for the early Rhuddanian), followed by that in the Tianlin section (−3.03‰ for the late Katian, and −4.50‰ for the early Rhuddanian). The highest values were observed in the Shuanghe section (0.25‰ for the late Katian, and 6.55‰ for the early Rhuddanian) (**Figure 9**). This distribution trend of $\delta^{34}S_{py}$ was consistent with the change in the paleowater depth and paleosalinity.

Therefore, it is inferred that in the pre-glacial and postglacial periods, detrital sulfate was mainly derived from the Chuangzhong and the Qianzhong Uplifts and precipitated in the shallow paleo-water of the Changhebian and Tianlin areas, respectively, as sulfides by microbial processes, to generate low $\delta^{34}S$ authigenic pyrite (**Figure 11A,C**). The Shuanghe section, located in the sedimentary depocenter, is far away from the source, limiting the supply of sulfate and resulting in ferruginous conditions (**Figure 11A,C**).

5.5.2 Hirnantian Glaciation

In the early Hirnantian (*M. extraordinarius* zone) stage, obvious euxinic water appeared in the Shuanghe section, but not in the Changhebian and Tianlin sections (**Figures 9**, **11B**). As mentioned previously, euxinic acid formed because of the increased availability of sulfate. Although the glacial period may reduce the intensity of chemical weathering, the sea-level fall forces continental shelf sediments rich in pyrite to be exposed to water and undergo weathering, thereby increasing the sulfate input in the local area of the depocenter. This speculation is supported by a reduction in the Changhebian section in the *M. extraordinarius* zone and the absence of the GYQ Formation (**Figure 9**). With rising temperatures, melting of glaciers, and rising sea levels at the end of the Hirnantian stage, the source area of exposed water was reduced and far away from the depocenter, thereby reducing the sulfate input and reconverting water to ferruginous conditions (**Figure 11B**).

Significant indigenous $\delta^{34}S_{py}$ gradient changes occurred during the glaciation: $\delta^{34}S_{py}$ in the Changhebian, Tianlin, and Shuanghe sections were −3.8‰, 1.2‰, and 9.81‰ (**Tables 2**), respectively. This change cannot be attributed to the chemical jump that sediments undergo, which results in the limitation of sulfate in pore water, especially in the *M. extraordinarius* zone, and euxinic conditions occur in the depocenter. We speculate that the increase in $\delta^{34}S_{py}$ during the glacial period represents an increase in the sulfate isotope input to the depocenter. This inference is supported by the correlation of paleosalinity between the three sections. In the Hirnantian stage, the paleosalinity of the Changhebian and Tianlin sections decreased due to the glacier and sea-level fall, but the paleosalinity of the Shuanghe section increased gradually and reached the maximum in the *M. extraordinarius* zone (**Figure 8**). This indicates that during the glacial period, the main provenance area in the region changed from the Qianzhong Uplift to the Chuangzhong Uplift. More specifically, it changed to the area represented by the Changhebian section that was briefly exposed to the surface due to the decrease in the sea level. Sulfate from the Changhebian section was re-weathered and transported to the Shuanghe section, thereby increasing the sulfate flux and promoting the formation of euxinic acid (**Figure 11B**).

Collectively, climate change and terrigenous debris input control the effectiveness of sulfate, which is the main controlling factor for the change in redox conditions of marine water before and after the Hirnantian glacial period.

6 CONCLUSION

Lithology and concentrations of major elements, trace elements, and sulfur isotope of the Changhebian and Tianlin sections located in the southwest of the Upper Yangtze Basin were analyzed and compared with the Shuanghe section in the depocenter. The main influencing factors of the spatiotemporal distribution in the redox conditions were discussed. Comprehensive indicators show that the activity of sedimentary OM and the availability of sulfate are the main factors that controlled the redox conditions of the water column, especially euxinic changes during the glacial period. This inference is based on a similar tectonic background, water sealing degree, paleosalinity, and paleowater depth of the two studied sections. Our work reveals the complex control of terrestrial clastic inputs on the transformation of redox conditions in semi-confined basins.

DATA AVAILABILITY STATEMENT

The original contributions presented in the study are included in the article/**Supplementary Material**; further inquiries can be directed to the corresponding author.

AUTHOR CONTRIBUTIONS

Investigation, ZD; Methodology, ZW and CW; review and editing, XF; data curation, WZ and SC; writing original draft, ZD; funding acquisition, CW.

FUNDING

This study was funded by the National Natural Science Foundation of China (No. 41772129).

SUPPLEMENTARY MATERIAL

The Supplementary Material for this article can be found online at: https://www.frontiersin.org/articles/10.3389/feart.2022.934488/full#supplementary-material

REFERENCES

Adachi, M., Yamamoto, K., and Sugisaki, R. (1986). Hydrothermal Chert and Associated Siliceous Rocks from the Northern Pacific Their Geological Significance as Indication Od Ocean Ridge Activity. *Sediment. Geol.* 47, 125–148. doi:10.1016/0037-0738(86)90075-8

Algeo, T. J., Marenco, P. J., and Saltzman, M. R. (2016). Co-evolution of Oceans, Climate, and the Biosphere during the 'Ordovician Revolution': A Review. *Palaeogeogr. Palaeoclimatol. Palaeoecol.* 458, 1–11. doi:10.1016/j.palaeo.2016.05.015

Algeo, T. J., and Maynard, J. B. (2004). Trace-element Behavior and Redox Facies in Core Shales of Upper Pennsylvanian Kansas-type Cyclothems. *Chem. Geol.* 206, 289–318. doi:10.1016/j.chemgeo.2003.12.009

Algeo, T. J., and Rowe, H. (2012). Paleoceanographic Applications of Trace-Metal Concentration Data. *Chem. Geol.* 324-325, 6–18. doi:10.1016/j.chemgeo.2011.09.002

Algeo, T. J., and Tribovillard, N. (2009). Environmental Analysis of Paleoceanographic Systems Based on Molybdenum-Uranium Covariation. *Chem. Geol.* 268, 211–225. doi:10.1016/j.chemgeo.2009.09.001

Arz, H. W., Lamy, F., Pätzold, J., Müller, P. J., and Prins, M. (2003). Mediterranean Moisture Source for an Early-Holocene Humid Period in the Northern Red Sea. *Science* 300, 118–121. doi:10.1126/science.1080325

Bhatia, M. R., and Crook, K. A. W. (1986). Trace Element Characteristics of Graywackes and Tectonic Setting Discrimination of Sedimentary Basins. *Contr. Mineral. Pet.* 92, 181–193. doi:10.1007/BF00375292

Bradley, A. S., Leavitt, W. D., Schmidt, M., Knoll, A. H., Girguis, P. R., and Johnston, D. T. (2016). Patterns of Sulfur Isotope Fractionation during Microbial Sulfate Reduction. *Geobiology* 14, 91–101. doi:10.1111/gbi.12149

Brenchley, P. J., Carden, G. A., Hints, L., Kaljo, D., Marshall, J. D., Martma, T., et al. (2003). High-resolution Stable Isotope Stratigraphy of Upper Ordovician Sequences: Constraints on the Timing of Bioevents and Environmental Changes Associated with Mass Extinction and Glaciation. *Geol. Soc. Am. Bull.* 115, 89–104. doi:10.1130/0016-7606(2003)115<0089:hrsiso>2.0.co;2

Caineng, Z., Zhi, Y., Songqi, P., Yanyan, C., Senhu, L., Jinliang, H., et al. (2016). Shale Gas Formation and Occurrence in China: An Overview of the Current Status and Future Potential. *Acta Geol. Sin. - Engl. Ed.* 90, 1249–1283. doi:10.1111/1755-6724.12769

Cawood, P. A., Hawkesworth, C. J., and Dhuime, B. (2012). Detrital Zircon Record and Tectonic Setting. *Geology* 40, 875–878. doi:10.1130/G32945.1

Chen, X., Rong, J., Li, Y., and Boucot, A. J. (2004). Facies Patterns and Geography of the Yangtze Region, South China, through the Ordovician and Silurian Transition. *Palaeogeogr. Palaeoclimatol. Palaeoecol.* 204, 353–372. doi:10.1016/S0031-0182(03)00736-3

Clarkson, M. O., Poulton, S. W., Guilbaud, R., and Wood, R. A. (2014). Assessing the Utility of Fe/Al and Fe-Speciation to Record Water Column Redox Conditions in Carbonate-Rich Sediments. *Chem. Geol.* 382, 111–122. doi:10.1016/j.chemgeo.2014.05.031

Cottle, J. M., Jessup, M. J., Newell, D. L., Horstwood, M. S. A., Noble, S. R., Parrish, R. R., et al. (2009). Geochronology of Granulitized Eclogite from the Ama Drime Massif: Implications for the Tectonic Evolution of the South Tibetan Himalaya. *Tectonics* 28, a–n. doi:10.1029/2008TC002256

Cox, R., Lowe, D. R., and Cullers, R. L. (1995). The Influence of Sediment Recycling and Basement Composition on Evolution of Mudrock Chemistry in the Southwestern United States. *Geochimica Cosmochimica Acta* 59 (14), 2919–2940. doi:10.1016/0016-7037(95)00185-9

Cullers, R. L., and Podkovyrov, V. N. (2002). The Source and Origin of Terrigenous Sedimentary Rocks in the Mesoproterozoic Ui Group, Southeastern Russia. *Precambrian Res.* 117, 157–183. doi:10.1016/S0301-9268(02)00079-7

Cullers, R., and Podkovyrov, V. N. (2000). Geochemistry of the Mesoproterozoic Lakhanda Shales in Southeastern Yakutia, Russia: Implications for Mineralogical and Provenance Control, and Recycling. *Precambrian Res.* 104, 77–93. doi:10.1016/S0301-9268(00)00090-5

Delabroye, A., and Vecoli, M. (2010). The End-Ordovician Glaciation and the Hirnantian Stage: A Global Review and Questions about Late Ordovician Event Stratigraphy. *Earth-Science Rev.* 98, 269–282. doi:10.1016/j.earscirev.2009.10.010

Gallego-Torres, D., Martínez-Ruiz, F., Paytan, A., Jiménez-Espejo, F. J., and Ortega-Huertas, M. (2007). Pliocene-Holocene Evolution of Depositional Conditions in the Eastern Mediterranean: Role of Anoxia vs. Productivity at Time of Sapropel Deposition. *Palaeogeogr. Palaeoclimatol. Palaeoecol.* 246, 424–439. doi:10.1016/j.palaeo.2006.10.008

Ge, T., Pan, J., Wang, K., Liu, W., Mou, P., and Wang, X. (2020). Heterogeneity of Pore Structure of Late Paleozoic Transitional Facies Coal-Bearing Shale in the Southern North China and its Main Controlling Factors. *Mar. Petroleum Geol.* 122, 104710. doi:10.1016/j.marpetgeo.2020.104710

Gomes, M. L., and Hurtgen, M. T. (2015). Sulfur Isotope Fractionation in Modern Euxinic Systems: Implications for Paleoenvironmental Reconstructions of Paired Sulfate-Sulfide Isotope Records. *Geochimica Cosmochimica Acta* 157, 39–55. doi:10.1016/j.gca.2015.02.031

Hammarlund, E. U., Dahl, T. W., Harper, D. A. T., Bond, D. P. G., Nielsen, A. T., Bjerrum, C. J., et al. (2012). A Sulfidic Driver for the End-Ordovician Mass Extinction. *Earth Planet. Sci. Lett.* 331-332, 128–139. doi:10.1016/j.epsl.2012.02.024

Hayashi, K. I., Fujisawa, H., Holland, H. D., and Ohmoto, H. (1997). Geochemistry of Approximately 1.9 Ga Sedimentary Rocks from Northeastern Labrador, Canada. *Geochim. Cosmochim. Acta* 61, 4115–4137. doi:10.1016/S0016-7037(97)00214-7

Hofmann, A. (2005). The Geochemistry of Sedimentary Rocks from the Fig Tree Group, Barberton Greenstone Belt: Implications for Tectonic, Hydrothermal and Surface Processes during Mid-archaean Times. *Precambrian Res.* 143, 23–49. doi:10.1016/j.precamres.2005.09.005

Hu, T., Pang, X., Jiang, S., Wang, Q., Xu, T., Lu, K., et al. (2018). Impact of Paleosalinity, Dilution, Redox, and Paleoproductivity on Organic Matter Enrichment in a Saline Lacustrine Rift Basin: A Case Study of Paleogene Organic-Rich Shale in Dongpu Depression, Bohai Bay Basin, Eastern China. *Energy fuels.* 32, 5045–5061. doi:10.1021/acs.energyfuels.8b00643

Jin, C., Li, C., Algeo, T. J., Planavsky, N. J., Cui, H., Yang, X., et al. (2016). A Highly Redox-Heterogeneous Ocean in South China during the Early Cambrian (~529-514 Ma): Implications for Biota-Environment Co-evolution. *Earth Planet. Sci. Lett.* 441, 38–51. doi:10.1016/j.epsl.2016.02.019

Johnston, D. T., Poulton, S. W., Dehler, C., Porter, S., Husson, J., Canfield, D. E., et al. (2010). An Emerging Picture of Neoproterozoic Ocean Chemistry: Insights from the Chuar Group, Grand Canyon, USA. *Earth Planet. Sci. Lett.* 290, 64–73. doi:10.1016/j.epsl.2009.11.059

Katz, B., and Lin, F. (2014). Lacustrine Basin Unconventional Resource Plays: Key Differences. *Mar. Petroleum Geol.* 56, 255–265. doi:10.1016/j.marpetgeo.2014.02.013

Leavitt, W. D., Halevy, I., Bradley, A. S., and Johnston, D. T. (2013). Influence of Sulfate Reduction Rates on the Phanerozoic Sulfur Isotope Record. *Proc. Natl. Acad. Sci. U.S.A.* 110, 11244–11249. doi:10.1073/pnas.1218874110

Li, C., Planavsky, N. J., Shi, W., Zhang, Z., Zhou, C., Cheng, M., et al. (2015). Ediacaran Marine Redox Heterogeneity and Early Animal Ecosystems. *Sci. Rep.* 5, 17097. doi:10.1038/srep17097

Li, N., Li, C., Algeo, T. J., Cheng, M., Jin, C., Zhu, G., et al. (2021a). Redox Changes in the Outer Yangtze Sea (South China) through the Hirnantian Glaciation and Their Implications for the End-Ordovician Biocrisis. *Earth-Science Rev.* 212, 103443. doi:10.1016/j.earscirev.2020.103443

Li, N., Li, C., Fan, J., Algeo, T. J., Yan, D., Zhu, G., et al. (2019). Sulfate-controlled Marine Euxinia in the Semi-restricted Inner Yangtze Sea (South China) during the Ordovician-Silurian Transition. *Palaeogeogr. Palaeoclimatol. Palaeoecol.* 534, 109281. doi:10.1016/j.palaeo.2019.109281

Li, Y., Zhang, T., Ellis, G. S., and Shao, D. (2017). Depositional Environment and Organic Matter Accumulation of Upper Ordovician-Lower Silurian Marine Shale in the Upper Yangtze Platform, South China. *Palaeogeogr. Palaeoclimatol. Palaeoecol.* 466, 252–264. doi:10.1016/j.palaeo.2016.11.037

Li, Y., Zhang, T., Shen, B., Li, Z., Shao, D., and Lash, G. G. (2021b). Carbon and Sulfur Isotope Variations through the Upper Ordovician and Lower Silurian of South China Linked to Volcanism. *Palaeogeogr. Palaeoclimatol. Palaeoecol.* 567, 110285. doi:10.1016/j.palaeo.2021.110285

Liang, D., Guo, T., Bian, L., Chen, J., and Zhao, Z. (2009). Some Progresses on Studies of Hydrocarbon Generation and Accumulation in Marine Sedimentary Regions, Southern China (Part 3): Controlling Factors on the Sedimentary Facies and Development of Palaeozoic Marine Source Rocks. *Mar. Orig. Pet. Geol.* 14, 1–19. doi:10.3969/j.issn.1672-9854.2009.02.001

Liu, Y., Li, C., Algeo, T. J., Fan, J., and Peng, P. a. (2016). Global and Regional Controls on Marine Redox Changes across the Ordovician-Silurian Boundary in South China. *Palaeogeogr. Palaeoclimatol. Palaeoecol.* 463, 180–191. doi:10.1016/j.palaeo.2016.10.006

Liu, Y., Li, C., Fan, J., Peng, P. a., and Algeo, T. J. (2020). Elevated Marine Productivity Triggered Nitrogen Limitation on the Yangtze Platform (South China) during the Ordovician-Silurian Transition. *Palaeogeogr. Palaeoclimatol. Palaeoecol.* 554, 109833. doi:10.1016/j.palaeo.2020.109833

Liu, Y., Siebel, W., Massonne, H. J., and Xiao, X. (2007). Geochronological and Petrological Constraints for Tectonic Evolution of the Central Greater Himalayan Sequence in the Kharta Area, Southern Tibet. *J. Geol.* 115, 215–230. doi:10.1086/510806

Lu, B., Qiu, Z., Zhang, B. H., Li, J., and Tao, H. F. (2021). Geological Significance of Rare Earth Elements in Marine Shale during the Late Ordovician-Early Silurian in Sichuan Basin, South China. *Geol. J.* 56, 1821–1840. doi:10.1002/gj.4027

Luening, S., Craig, J., Loydell, D. K., Storch, P., and Fitches, B. (2000). Lower Silurian "hot Shales" in North Africa and Arabia; Regional Distribution and Depositional Model. *Earth-Sci Rev.* 49, 121–200. doi:10.1016/S0012-8252(99)00060-4

McLennan, S. M. (2001). Relationships between the Trace Element Composition of Sedimentary Rocks and Upper Continental Crust. *Geochem. Geophys. Geosystems* 2, n/a. doi:10.1029/2000gc000109

Mort, H., Jacquat, O., Adatte, T., Steinmann, P., Föllmi, K., Matera, V., et al. (2007). The Cenomanian/Turonian Anoxic Event at the Bonarelli Level in Italy and Spain: Enhanced Productivity And/or Better Preservation? *Cretac. Res.* 28, 597–612. doi:10.1016/j.cretres.2006.09.003

Mou, G., Ge, X., Yu, Q., Men, X., Liu, W., He, J., et al. (2019). Palaeoclimatology and Provenance of Black Shales From Wufeng-Longmaxi Formations in Southwestern Sichuan Province: From Geochemical Records of Well Xindi-2 *Journal of Palaeogeography* 21, 835–854. doi:10.7605/gdlxb.2019.05.057

Mou, G., Wang, X., Wang, Q., Zhou, K., Liang, W., Ge, X., et al. (2016). Relationship Between Sedimentary Facies and Shale Gas Geological Conditions of the Lower Silurian Longmaxi Formation in southern Sichuan Basin and its Adjacent Areas *Journal of Palaeogeography* 18, 457–472. doi:10.7605/gdlxb.2016.03.032

Mu, C., Zhou, K., Liang, W., and Ge, X. (2011). Early Paleozoic Sedimentary Environment of Hydrocarbon Source Rocks in the Middle-Upper Yangtze Region and Petroleum and Gas Exploration. *ACTA Geol. Sin.* 85, 526–532. doi:10.1016/S1876-3804(14)60082-3

Murray, R. W. (1994). Chemical Criteria to Identify the Depositional Environment of Chert: General Principles and Applications. *Sediment. Geol.* 90, 213–232. doi:10.1016/0037-0738(94)90039-6

Nesbitt, H. W., and Young, G. M. (1982). Early Proterozoic Climates and Plate Motions Inferred from Major Element Chemistry of Lutites. *Nature* 299, 715–717. doi:10.1038/299715a0

Pan, J., Ge, T., Liu, W., Wang, K., Wang, X., Mou, P., et al. (2021). Organic Matter Provenance and Accumulation of Transitional Facies Coal and Mudstone in Yangquan, China: Insights from Petrology and Geochemistry. *J. Nat. Gas Sci. Eng.* 94, 104076. doi:10.1016/j.jngse.2021.104076

Panahi, A., Young, G. M., and Rainbird, R. H. (2000). Behavior of Major and Trace Elements (Including REE) during Paleoproterozoic Pedogenesis and Diagenetic Alteration of an Archean Granite Near Ville Marie, Québec, Canada. *Geochimica Cosmochimica Acta* 64, 2199–2220. doi:10.1016/S0016-7037(99)00420-2

Poulton, S. W., and Canfield, D. E. (2011). Ferruginous Conditions: A Dominant Feature of the Ocean through Earth's History. *Elements* 7, 107–112. doi:10.2113/gselements.7.2.107

Raiswell, R., and Canfield, D. E. (2012). The Iron Biogeochemical Cycle Past and Present. *GeochemPersp* 1, 1–220. doi:10.7185/geochempersp.1.1

Sageman, B. B., Murphy, A. E., Werne, J. P., Ver Straeten, C. A., Hollander, D. J., and Lyons, T. W. (2003). A Tale of Shales: the Relative Roles of Production, Decomposition, and Dilution in the Accumulation of Organic-Rich Strata, Middle-Upper Devonian, Appalachian Basin. *Chem. Geol.* 195, 229–273. doi:10.1016/S0009-2541(02)00397-2

Saltzman, M. R., and Young, S. A. (2005). Long-lived Glaciation in the Late Ordovician? Isotopic and Sequence-Stratigraphic Evidence from Western Laurentia. *Geol* 33, 109–112. doi:10.1130/G21219.1

Schoepfer, S. D., Shen, J., Wei, H., Tyson, R. V., Ingall, E., and Algeo, T. J. (2015). Total Organic Carbon, Organic Phosphorus, and Biogenic Barium Fluxes as Proxies for Paleomarine Productivity. *Earth-Science Rev.* 149, 23–52. doi:10.1016/j.earscirev.2014.08.017

Sugitani, K., Yamashita, F., Nagaoka, T., Yamamoto, K., Minami, M., Mimura, K., et al. (2006). Geochemistry and Sedimentary Petrology of Archean Clastic Sedimentary Rocks at Mt. Goldsworthy, Pilbara Craton, Western Australia: Evidence for the Early Evolution of Continental Crust and Hydrothermal Alteration. *Precambrian Res.* 147, 124–147. doi:10.1016/j.precamres.2006.02.006

Taylor, S. R., and McClcnnan, S. M. (1985). *The Continental Crust: Its Composition and Evolution*. United States: OSTI.GOV.

Tribovillard, N., Algeo, T. J., Baudin, F., and Riboulleau, A. (2012). Analysis of Marine Environmental Conditions Based Onmolybdenum-Uranium Covariation-Applications to Mesozoic Paleoceanography. *Chem. Geol.* 324-325, 46–58. doi:10.1016/j.chemgeo.2011.09.009

Tribovillard, N., Algeo, T. J., Lyons, T., and Riboulleau, A. (2006). Trace Metals as Paleoredox and Paleoproductivity Proxies: An Update. *Chem. Geol.* 232, 12–32. doi:10.1016/j.chemgeo.2006.02.012

Wang, C., Dong, Z., Fu, X., Chen, Q., Liu, X., Tang, M., et al. (2021). Spatiotemporal Evolution and Genesis of the Late Ordovician-Early Silurian Marine Euxinia in Northeastern Upper Yangtze Basin, South China. *Front. Earth Sci.* 9, 788349. doi:10.3389/feart.2021.788349

Wang, Q., Jiang, F., Ji, H., Jiang, S., Liu, X., Zhao, Z., et al. (2020). Effects of Paleosedimentary Environment on Organic Matter Enrichment in a Saline Lacustrine Rift Basin - A Case Study of Paleogene Source Rock in the Dongpu Depression, Bohai Bay Basin. *J. Petroleum Sci. Eng.* 195, 107658. doi:10.1016/j.petrol.2020.107658

Wei, W., and Algeo, T. J. (2020). Elemental Proxies for Paleosalinity Analysis of Ancient Shales and Mudrocks. *Geochimica Cosmochimica Acta* 287, 341–366. doi:10.1016/j.gca.2019.06.034

Wersin, P., Höhener, P., Giovanoli, R., and Stumm, W. (1991). Early Diagenetic Influences on Iron Transformations in a Freshwater Lake Sediment. *Chem. Geol.* 90, 233–252. doi:10.1016/0009-2541(91)90102-W

Yan, D., Chen, D., Wang, Q., and Wang, J. (2009). Geochemical Changes across the Ordovician-Silurian Transition on the Yangtze Platform, South China. *Sci. China Ser. D-Earth Sci.* 52, 38–54. doi:10.1007/s11430-008-0143-z

Yan, D., Chen, D., Wang, Q., and Wang, J. (2010). Large-scale Climatic Fluctuations in the Latest Ordovician on the Yangtze Block, South China. *Geology* 38, 599–602. doi:10.1130/G30961.1

Zaid, S. M. (2015). Geochemistry of Sandstones from the Pliocene Gabir Formation, North Marsa Alam, Red Sea, Egypt: Implication for Provenance, Weathering and Tectonic Setting. *J. Afr. Earth Sci.* 102, 1–17. doi:10.1016/j.jafrearsci.2014.10.016

Zhang, K., Jin, W., Lin, H., Dong, C., and Wu, S. (2018). Major and Trace Elemental Compositions of the Upper Carboniferous Batamayineishan Mudrocks, Wulungu Area, Junggar Basin, China: Implications for Controls on the Formation of the Organic-Rich Source Rocks. *Mar. Petroleum Geol.* 91, 550–561. doi:10.1016/j.marpetgeo.2018.01.003

Zhou, L., Algeo, T. J., Shen, J., Hu, Z., Gong, H., Xie, S., et al. (2015). Changes in Marine Productivity and Redox Conditions during the Late Ordovician Hirnantian Glaciation. *Palaeogeogr. Palaeoclimatol. Palaeoecol.* 420, 223–234. doi:10.1016/j.palaeo.2014.12.012

Zou, C., Qiu, Z., Poulton, S. W., Dong, D., Wang, H., Chen, D., et al. (2018). Ocean Euxinia and Climate Change "Double Whammy" Drove the Late Ordovician Mass Extinction. *Geol. (Boulder)* 46, 535–538. doi:10.1130/g40121.1

Conflict of Interest: The authors declare that the research was conducted in the absence of any commercial or financial relationships that could be construed as a potential conflict of interest.

Publisher's Note: All claims expressed in this article are solely those of the authors and do not necessarily represent those of their affiliated organizations, or those of the publisher, the editors, and the reviewers. Any product that may be evaluated in this article, or claim that may be made by its manufacturer, is not guaranteed or endorsed by the publisher.